4^{th} QUARTERLY PROJECT STATUS REPORT

Project Title: Effects of Calcium Magnesium Acetate on the Combustion of Coal-Water Slurries

DOE/PC/89776--1

DE91 002607

DOE Grant #: DE-FG22-89PC89776

Principal Investigator: Yiannis A. Levendis

Project Performance Period: 1 June 1990 - 31 August 1990

Project Objectives:

The general objective of the project is to investigate the combustion behavior of single and multiple Coal-Water Slurry particles burning at high temperature environments. Both uncatalyzed as well as catalyzed CWS drops with Calcium Magnesium Acetate (CMA) catalyst will be investigated. Emphasis will also be given in the effects of CMA on the sulfur capture during combustion. To help achieve these objectives the following project tasks were carried over this $4th$ three-month period.

Project Tasks:

1 MODELLING OF THE EVAPORATION, HEAT-UP AND DEVOLATILIZATION PERIODS FOR COAL-WATER, ETHANOL-WATER and ACETONE-WATER SLURRIES

Pure Liquid Drops

In this part of the investigation we used numerical modelling to explore the evaporation and heatup behavior of a spectrum of droplets in the reactor. The size of droplets ranged between 50 and 500μm and their composition was varied to include suspensions of coal in water, ethanol or acetone. The gas phase conditions

were chosen before introduction of a dispersed phase (droplet), as described in the previous report. Calculations were performed with injector flowrates set to 0.1 slpm, where velocity and temperature profiles are disturbed minimally by the injector flow.

Particle trajectories for coal-water droplets are shown in Fig. 1 a-d. The model predicts that particles smaller than 100μm evaporate completely by the time they reach the tip of the particle injector. Particles that are between 100 and 350μm evaporate inside the radiation cavity. Particles that are >350μm leave the furnace still wet, and therefore, their combustion study in this apparatus does not appear feasible.

Evaporation of ethanol droplets turned out to be a little faster, as expected, but only to an insignificant degree as far as the present study is concerned, Fig. 1 e-h. The case of pure acetone drops was also studied, and the trajectories are presented in Fig. 2 a-d. For a given initial droplet diameter the numerical solution predicted that in the case of acetone drops the evaporation phase would end significantly closer to the tip of the injector. Also a 450 μm drop would be completely vaporized inside the furnace. This is important for studies of slurries in our system, whenever is desired to investigate the combustion of larger drops.

Slurry Drops

Numerically predicted trajectories of coal-water and coal-ethanol slurry drops are also shown in Figure 1, top and bottom rows, respectively, and for coal-acetone drops in Fig. 2. The axial positions in the furnace where the evaporation is completed are marked with solid asterisks. The initial drop size was set to vary between 50 and 350μm for water and ethanol and 100 and 450μm for acetone. The composition was set to 75% water and 25% solids. Upon completion of the evaporation phase the particles can either be allowed heat-up, or, if they are assumed to contain volatiles, a devolatilization stage will take place. In both cases the particle temperature increases rapidly to the prevailing gas temperature.

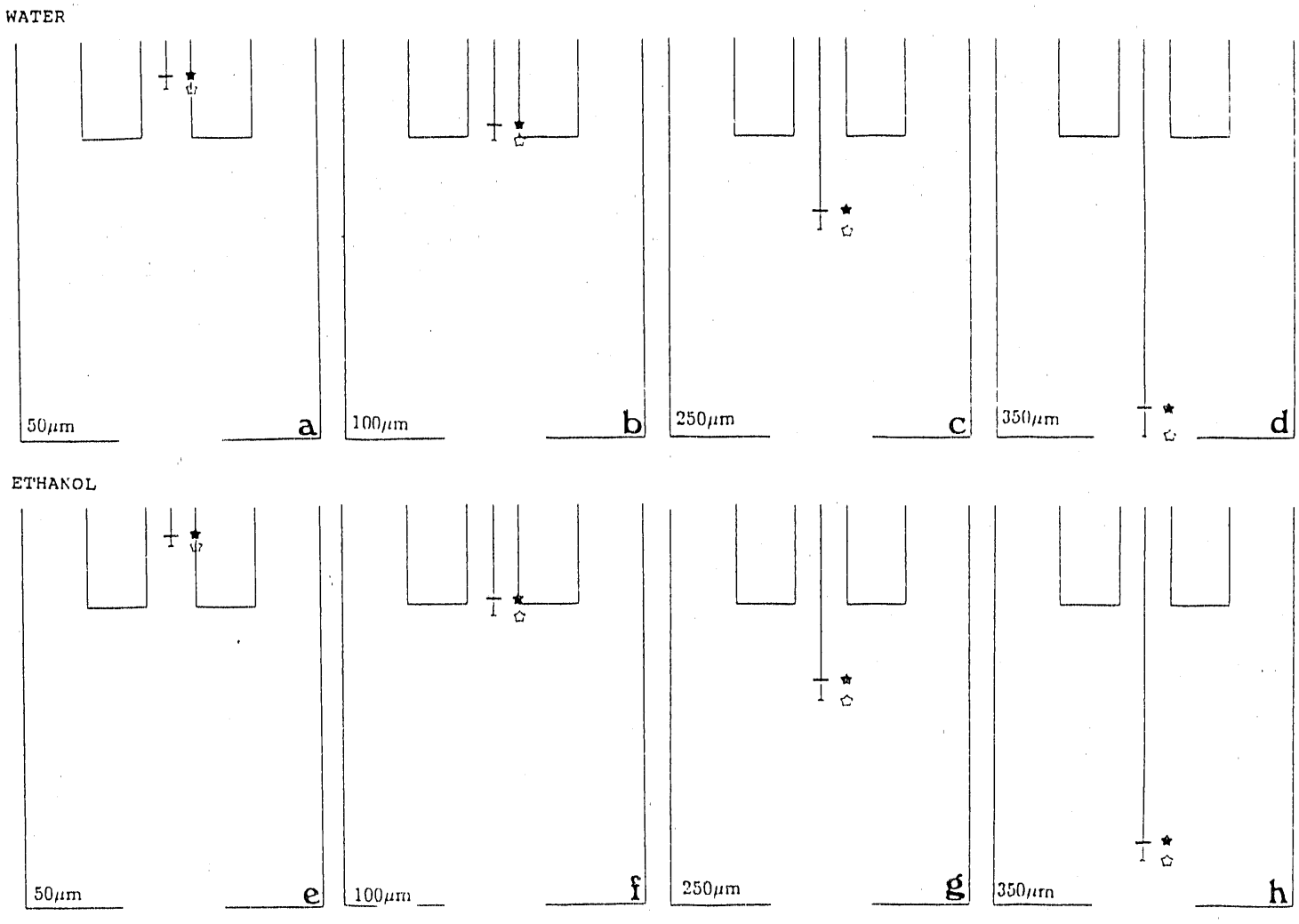

Figure 1: Numerical calculations of trajectories of evaporating water (or ethanol) (✡) and coal-water(or coal-ethanol) (★) drops. Injector flowrates at 0.1 slpm, combustion air flowrate at 2.0 slpm, wall temperature 1500 K.

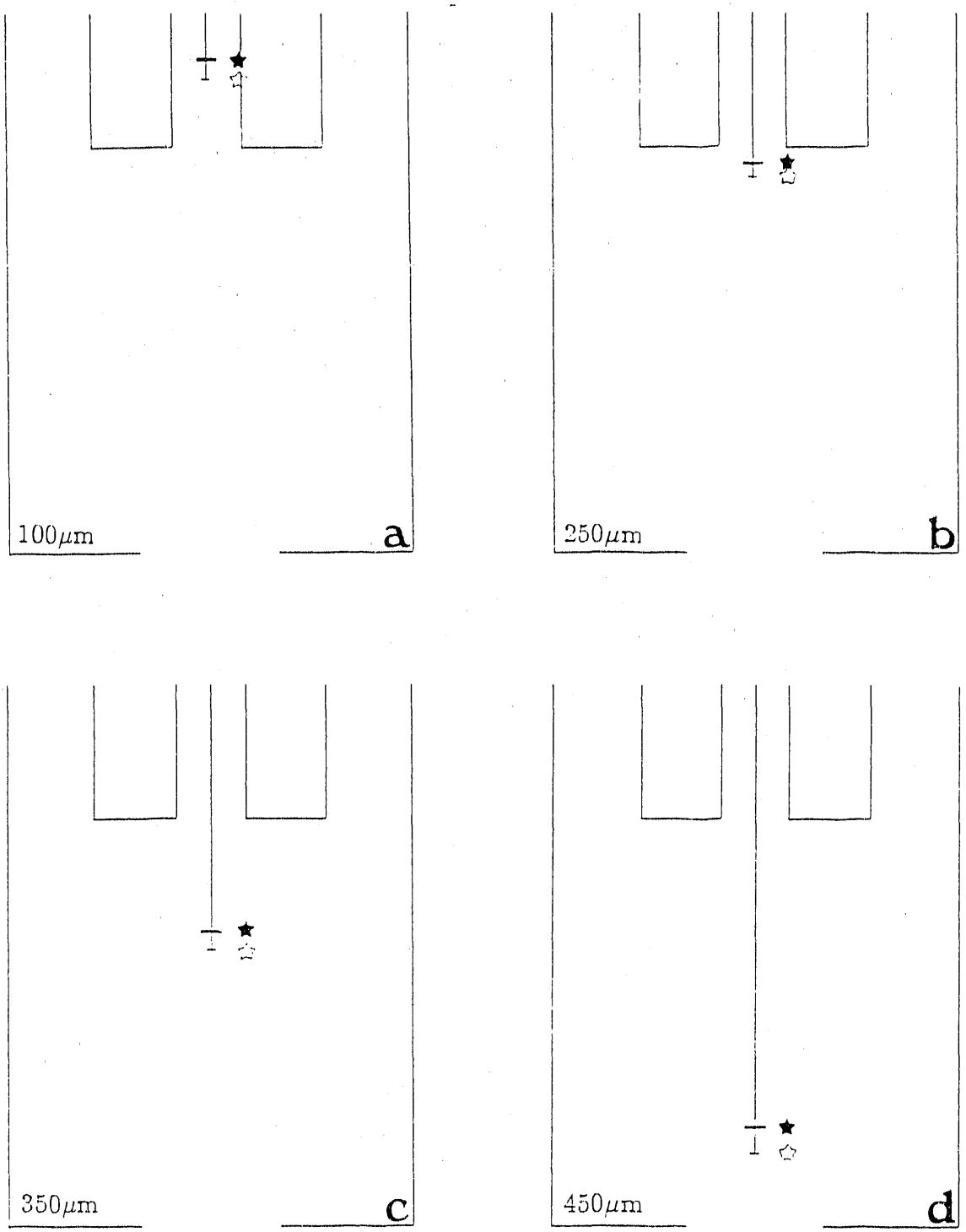

Figure 2: Numerical calculations of trajectories of evaporating acetone (✡) and coal-acetone (✸) drops. Injector flowrates at 0.1 slpm, combustion air flowrate at 2.0 slpm, wall temperature 1500 K.

In the latter case devolatilization occurs simultaneously with heat-up. For this calculation the volatiles were assumed to be propane. The average surface partial pressure of propane was assumed to be 0.5 atm, and the volatiles were supposed to diffuse in the surrounding gas without igniting. Devolatilization was set to commence at a temperature of 400 K. The average surface partial pressure was estimated based on devolatilization times for bituminous coals published in the literature. Droplet diameter-time and temperature-time plots for coal-water slurry drops are shown in Figures 3 and 4. The estimated devolatilization times varied between 1.7 and 23.4 ms for CWS droplets with initial sizes ranging between 50 and 250μm. The particle temperature at the completion of the devolatilization stage varied between 560 and 920 K for the above size range.

Thus, subsequent combustion events of the dried particles will commence at axial locations within the combustor that vary with the initial diameter of the CWS droplet. The larger the initial drop the further down in the furnace the remaining solid is going to burn. Thus, modelling of the combustion of slurry requires a complete knowledge of the gas phase environment. Results on Figs. 1-4 show that, under the conditions examined, evaporation for the 50μm drop takes 0.58 sec inside the injector, and for the faster falling 250μm drop takes a total of only 0.19 sec inside both the injector and the radiation cavity. This is a rather interesting result and it can readily explained on the grounds that faster moving, bigger particles enter the radiation zone immediately and evaporate at once under the intense heat existing there. Slow moving, small drops evaporate slowly inside the injector. Finally, it can be observed that the heat-up phase of fine particles ($< 100\mu$m) follows the climbing gas temperature profile closely. In contrast larger droplets ($> 100\mu$m) have penetrated into the radiation cavity deeply enough, that upon completion of vaporization they heat up rapidly to the asymptote of the gas temperature, Fig. 4. In the latter case subsequent char combustion takes place at constant gas temperature; in the former case gas temperature will be varying in the initial stages of combustion.

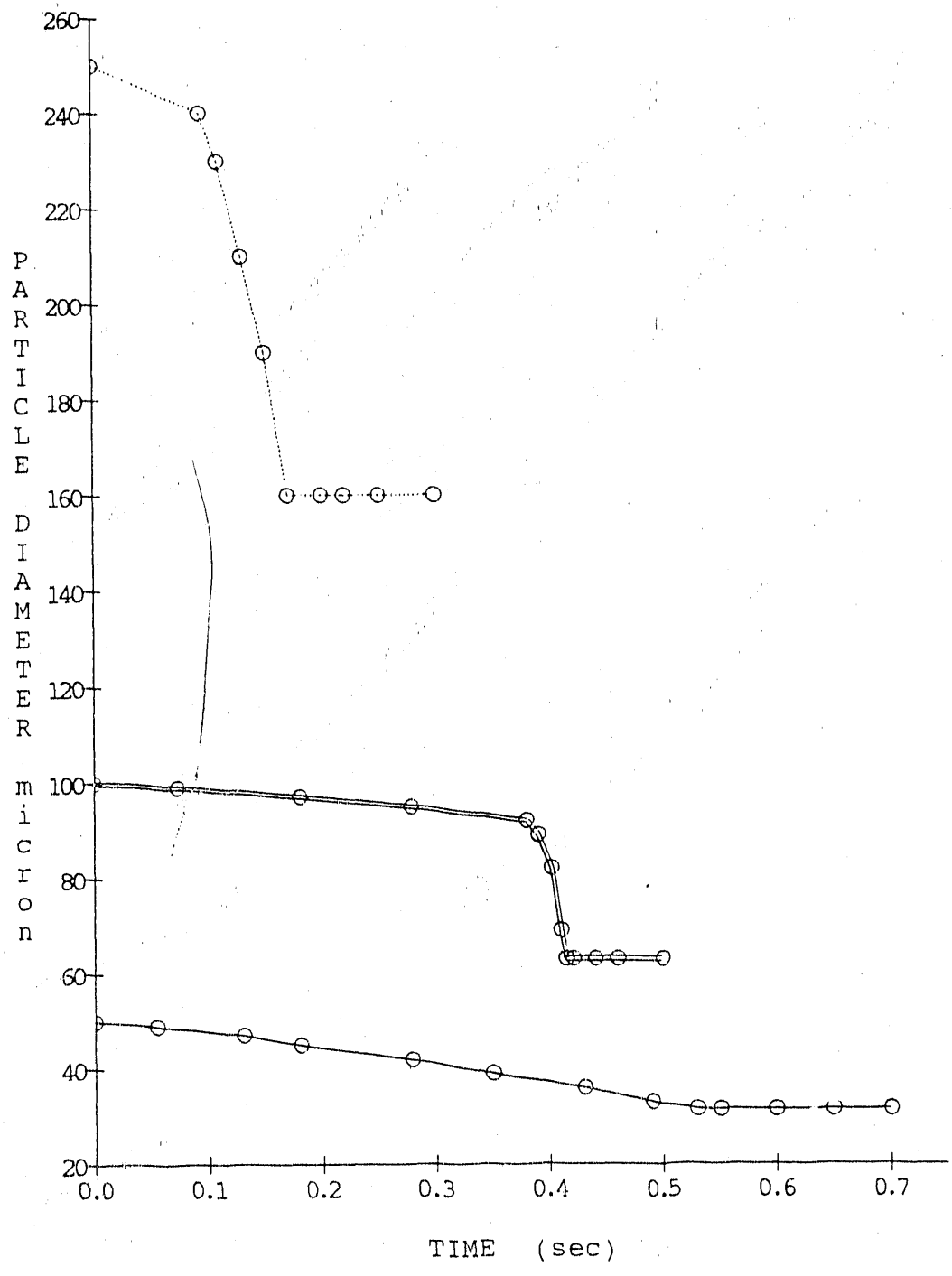

Figure 3: Particle diameter vs time for a coal-water slurry drop with 75% initial water content. Injector flow 0.1 slpm,combustion air 2.0 slpm, wall temperature 1500 K.

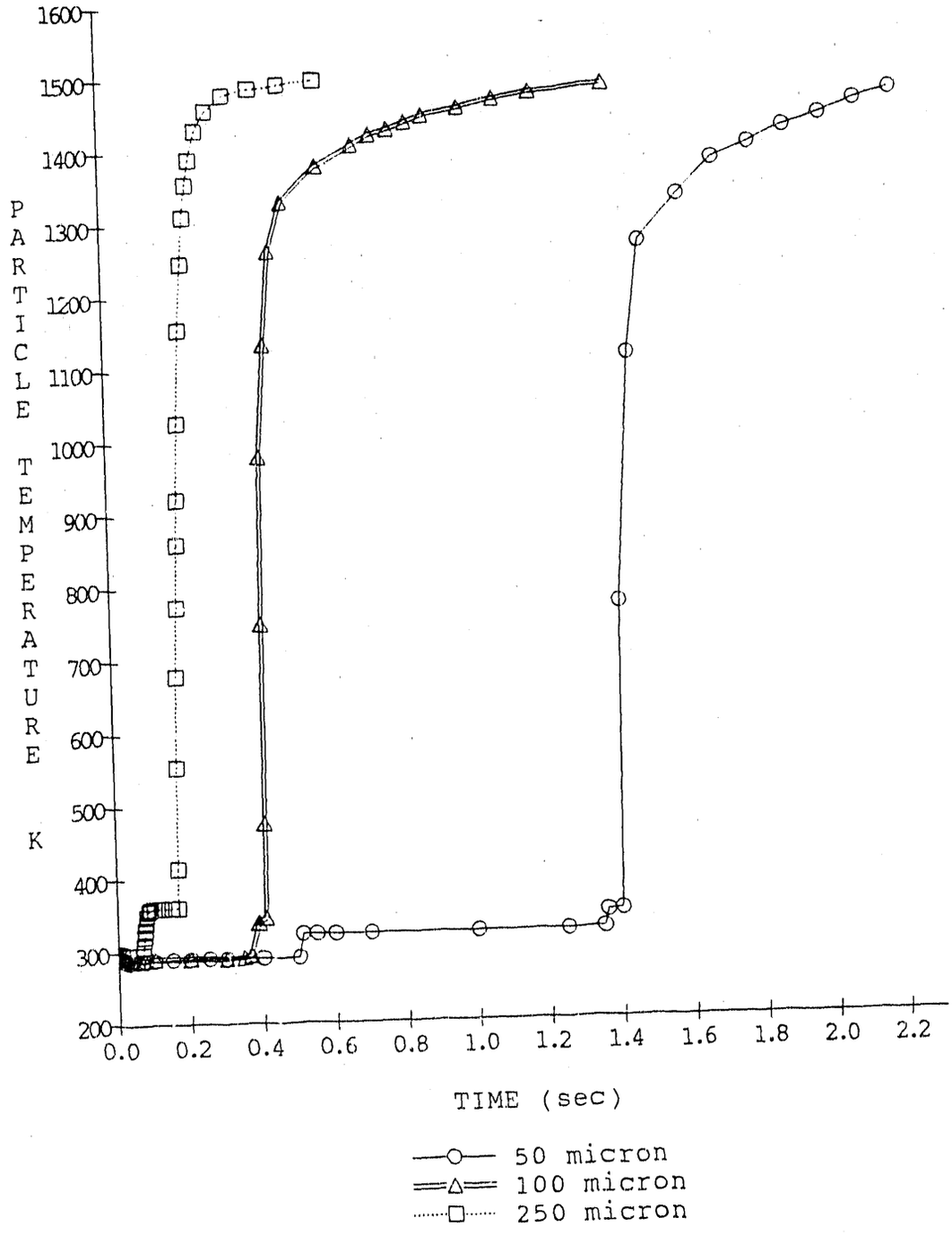

Figure 4: Particle temperature vs time for a coal-water slurry drop with 75% initial water content. Injector flow 0.1 slpm,combustion air 2.0 slpm, wall temperature 1500 K.

This part of the investigation is now considered completed.

2 GAS VELOCITY MEASUREMENTS - HOT WIRE ANEMOMETER

An attempt to measure the velocity in the furnace was also made. From the results of the numerical solution for the gas phase (shown in a previous report), it was predicted that positive (downward) axial centerline gas velocities, for the range of operating conditions proposed for the laminar flow reactor, would be in the range 15-70 cm/sec with gas temperatures of 500-1900 K. For this purpose a constant temperature hot wire anemometer probe was constructed, and is shown in Fig. 5, along with the suction thermometer. In this constant-temperature version of the instrument the current through the wire is adjusted to keep the wire temperature (as measured by its resistance) maintained approximately constant by a feedback circuit. The current required to do this then becomes a measure of flow velocity.

The most commonly used materials for hot wire sensors are tungsten, platinum and platinum alloys. Tungsten is popular because of its high tensile strength and high melting point. However, it has a rather low oxidation temperature which sets the upper limit for sensor operating temperature at 600 K. Platinum was the one selected for this application. Its tensile strength is lower than tungsten, but this is not significant for lower velocity flows. Its oxidation temperature is higher than tungsten and it may be used in air at an operating temperature up to 1400 K. Molybdenum was selected as the material for the support wires for the platinum wire because of its high melting temperature and fairly low resistivity.

A small diameter (typically 5μm) sensor is normally used to improve frequency response when measuring temperature or velocity fluctuations. The aspect ratio of the sensor should be in the range $200 < l/d < 400$ for best performance. In this case the diameter (d) was increased to 125 μm to extend the sensor operating life at high temperature and the length (l) was increased to 25 mm to maintain

an aspect ratio of 200. The increased mass of the wire is not significant as we are measuring mean velocity or temperature at steady state. No measurements were made above 900 K because the platinum element and the molybdenum leads were connected using silver solder which melted when the wall temperature exceeded this value.

Typical hot wire probe calibration curves show a marked decrease in sensitivity at low velocities. When a hot wire is placed in a quiescent fluid, convection currents are formed because of the buoyancy of the heated fluid. This free convection flow tends to mask any low-velocity forced convection cooling, resulting in a flattening of the lower end of the calibration curve. It has been determined elsewhere, that a lower-velocity limit for which the free convection component would cause no more than a 10% error in the calculation of the Reynolds number based on the forced convection velocity only. The lower limit is $Re = 9Ra^{0.418}$ for counter flow where free and forced convection oppose one another. The Rayleigh number, Ra, is defined as the product of the Grashof and Prandtl numbers. Using this formula we get u_{min} =15.0 cm/sec. Therefore under the operating conditions specified for the laminar down-flow reactor the hot-wire anemometer was operating near the lower limit imposed by free convection effects.

A calibration curve was obtained at 900 K with the instrument controlled by the electrical circuit shown in Fig. 5b. The bridge was first balanced with the platinum element in the furnace with no gas flow at 900 K. Then the platinum wire resistance, and therefore its temperature, was kept constant by a feedback circuit. The flow of combustion air entering the tube furnace was varied, with zero injector air flow, and the current change due to increased heat loss from the wire was measured. Separate gas temperature measurements were made which indicated that the gas temperature remained approximately constant during the calibration as long as the injector air flow was zero. To increase the sensitivity, the current output was converted to a voltage drop in a resistance, inserted in series with the platinum wire. This voltage was amplified using a transistor. The platinum

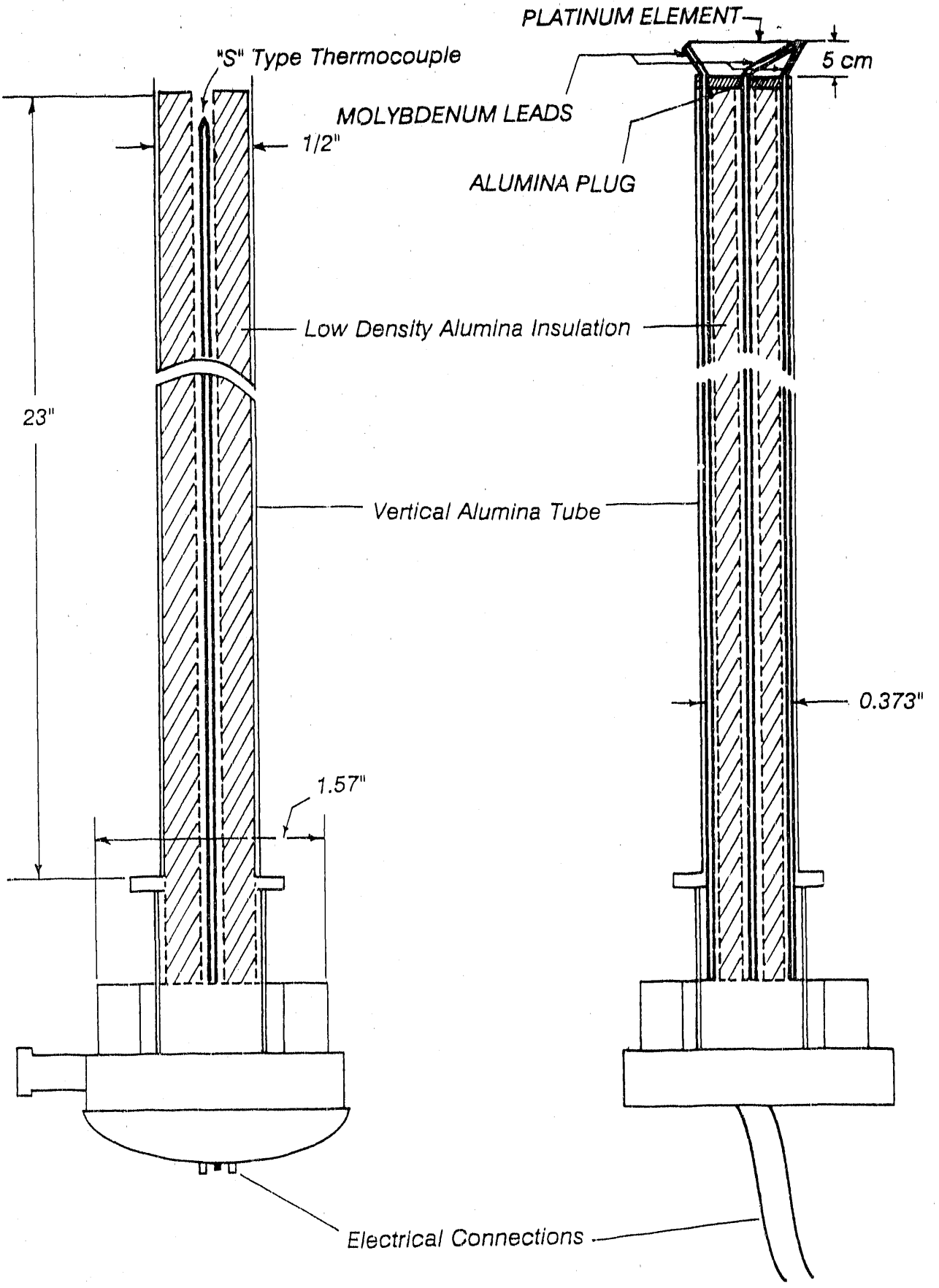

Figure 5a: Schematic of the suction thermometer and hot-wire anemometer probe.

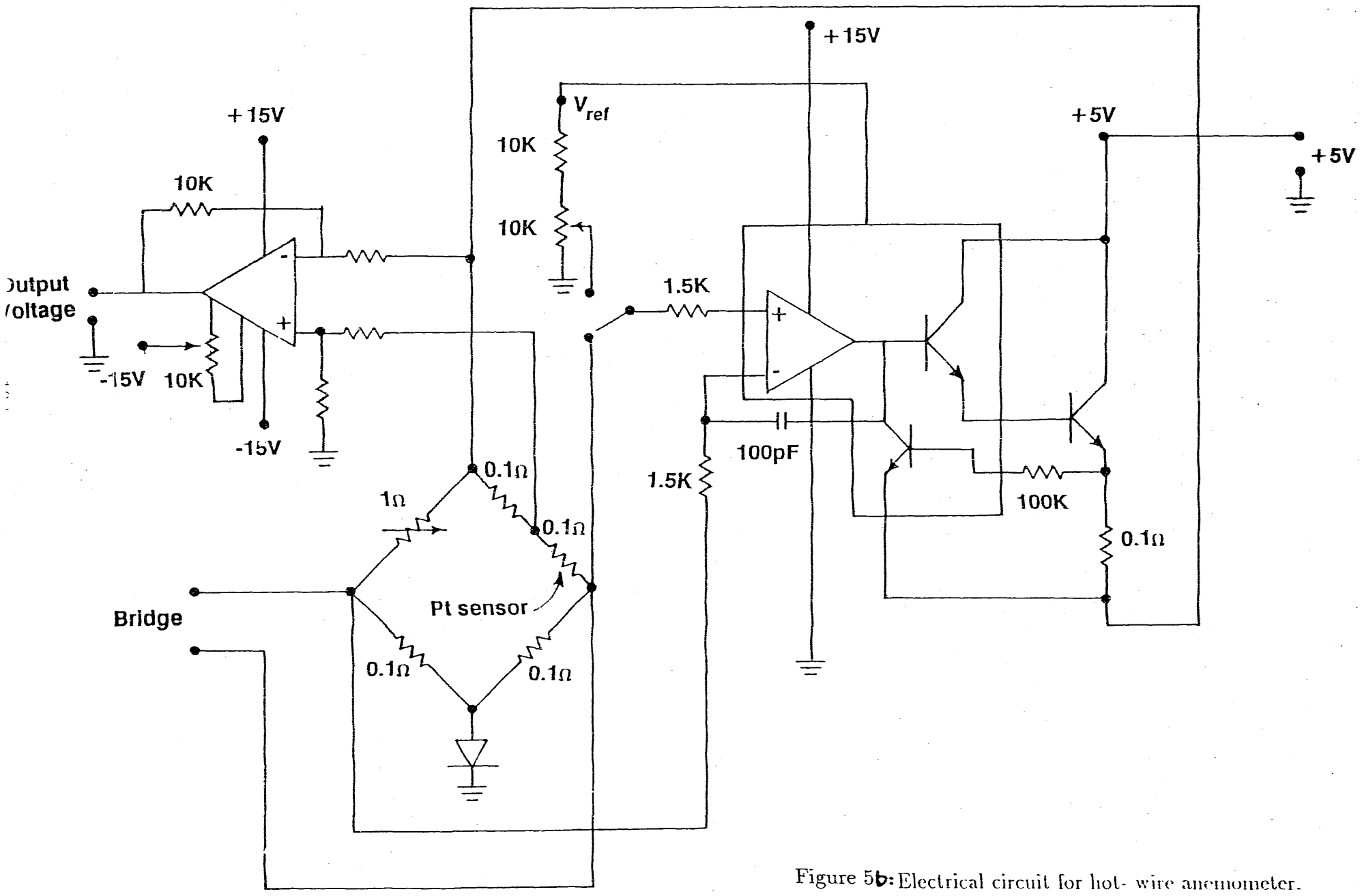

Figure 5b: Electrical circuit for hot- wire anemometer.

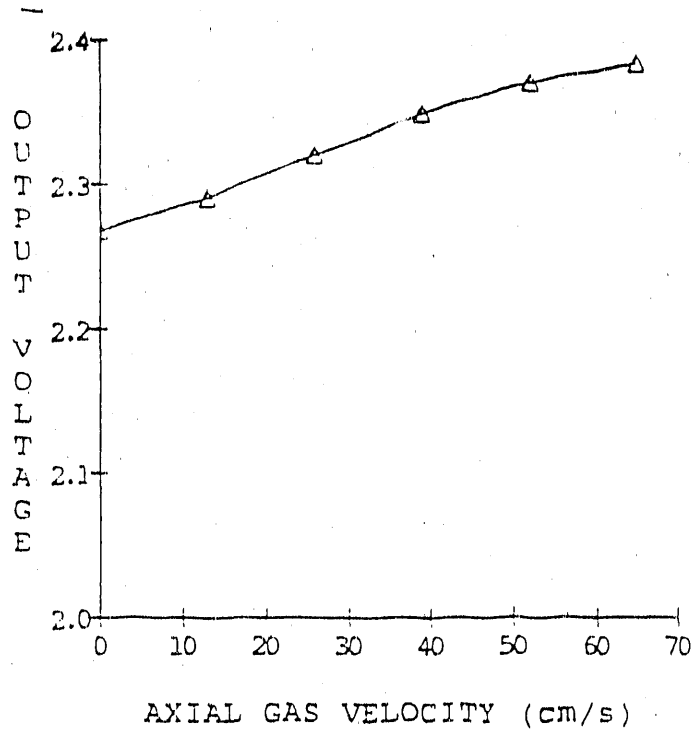

Figure 6: Average anemometer output voltage reading vs. gas velocity from calibration results at 900 K.

sensor wire was placed near the bottom of the hot zone on the centerline of the tube furnace. The gas velocity for the calibration was calculated assuming fully developed flow and a gas temperature of 900 K. The results of the calibration are presented in Table I. There was a rapid fluctuation in the voltage reading, probably due to the conflict between natural and forced convection modes of heat loss from the wire. The average velocity reported was not a true average, but the midpoint of the range of readings. The averages are plotted against the calibration gas velocity in Fig. 6. The curve is quite flat and the total change in voltage from zero to the maximum velocity is of the same order as the range of voltage fluctuation for each reading. Therefore it appears that this hot-wire anemometer, or at least this configuration, cannot give accurate readings at the low velocities encountered in our laminar down-flow reactor. Centerline axial velocity measurements were made using the calibration curve shown in Fig. 6, and the results compared to a numerical solution obtained at 900 K. The results for injector air flow rates of 0.1

Gas Velocity (cm/sec)	Output Range (volts)	Average Output (volts)
0.00	2.232-2.303	2.268
13.0	2.258-2.321	2.290
26.0	2.281-2.361	2.321
39.0	2.305-2.393	2.349
52.0	2.331-2.410	2.370
65.0	2.341-2.424	2.383

Table 1: Calibration results at 300 K for hot-wire anemometer

slpm and 0.5 slpm are presented in Fig. 7. The numerical solution predicts that the centerline axial velocity would show a maximum below the tip of the injector. The experimental velocity measurements are of the same order of magnitude as those predicted by the numerical solution. Given the aforementioned limitations in accuracy of the instrument, however, we cannot state definitely that the velocity did indeed show a maximum a certain distance below the injector.

3 DESIGN AND CONSTRUCTION OF AN OPTICAL PYROMETER.

Development of an optical pyrometer is a complex and time consuming task. It has been started quite some time ago and over this last three month period final stages of the construction took place.

OPTICS.

Light from the furnace is transmitted through a 1 mm diameter single fiber optic to the optical pyrometer assembly. The whole assembly is constructed on a 45 cm square optical table (*Newport*). Three rails are used to carry the optical components that conduct radiation to three detectors in the arrangement shown in Fig. 8. A special feature of this pyrometer is the use of two dichroic (cold mirror) beam splitters to direct the light to the detectors. These beam splitters have the advantage of allowing transmission of certain bands of wavelengths at

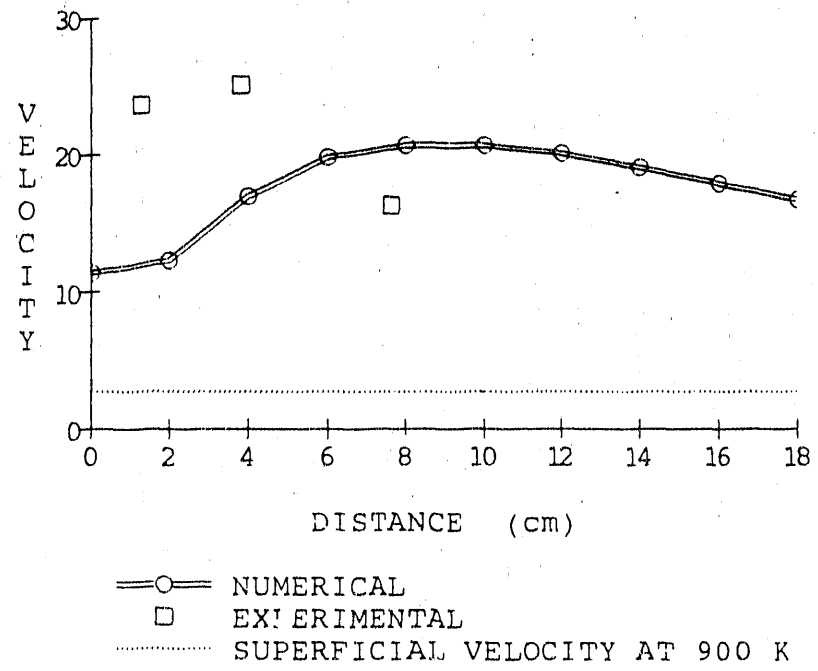

a

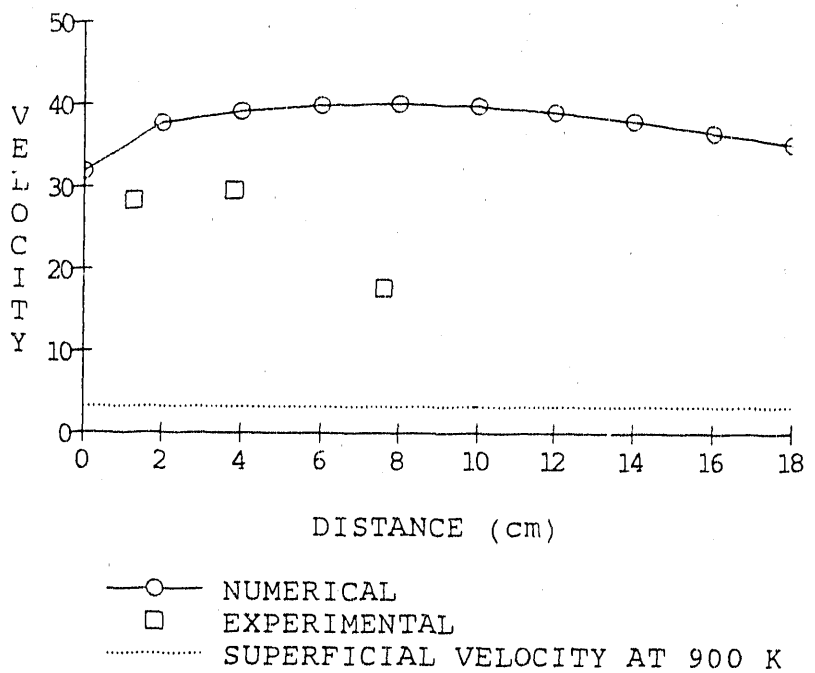

b

Figure 7: Experimental and numerical centerline axial velocity vs. distance from the tip of the injector. Injector air flow (a) 0.1 slpm (superficial velocity 2.73 cm/s) and (b) 0.5 slpm (superficial velocity 3.25 cm/s). Combustion air flow 2.0 slpm, wall temperature 900 K.

high efficiency (≈90%), while reflecting any other light. Thence, by optimal choice of dichroic - interference filter combinations the magnitude of the radiation carried to the detectors can be maximized. Since the cut-off wavelenths of the dichroic filters change with the angle of the incident radiation, care must be exercised in selecting the above combinations. This design is superior to a trifurcated optical fiber bundle for three reasons: (i) each detector receives approx. 90% of the total radiation, as explained above, in contrast to 33% of the trifurcated bundle, (ii) avoids the randomness of the light split among the detectors, and (iii) has better particle imaging properties than a bundle, as explained in the previous report.

The optical holders ride on three rails (30, 15, 15 cm long) and matching rail carriers and stands purchased from *Oriel*). The light-carrying optical fiber is fitted with a borosilicate glass collimator (*Oriel*) the same as the one fitted on the top of the furnace injector, and it is mounted on a special collimator mount. The light is thus carried to the first dichroic beam splitter which is mounted on a rotating stage (*Melles Griot*) at an angle of 53.5° dictated by the screw pattern of the optical table - rail combination. This filter (*Newport*) transmits above 850 nm and reflects lower wavelengths as shown in Fig. 9. A second dichroic filter (*Oriel*) is placed further along the light beam to split the remaining spectrum (transmitted from the first dichroic filter) to the other two detectors. The spectrum of this filter is shown in Fig. 10. Three narrow bandwidth (FWHM = 10 nm) interference filters (*Oriel*) are used to define the working wavelengths of 0.8, 0.975, and 1.2 um. In conjunction with these interference filters, three 19-mm- focal-length aspheric lenses are used to focus the light beams onto the photodetectors. Two Silicon and one Germanium photodetectors are used to transform the incident light into a voltage signal. At the present time we are experiencing difficulties with the germanium photodetectors. Details on the actions we are taking will be described in the next report. Also construction of the pyrometer electronics is almost complete and their description will also be given in the next report. Plans for the coming three month period include improving the performance of the pyrometer, complete the electronics

design and implement the data acquisition routines. For this purpose an IBM-AT has been obtained from the ME department exclusively for the needs of this project.

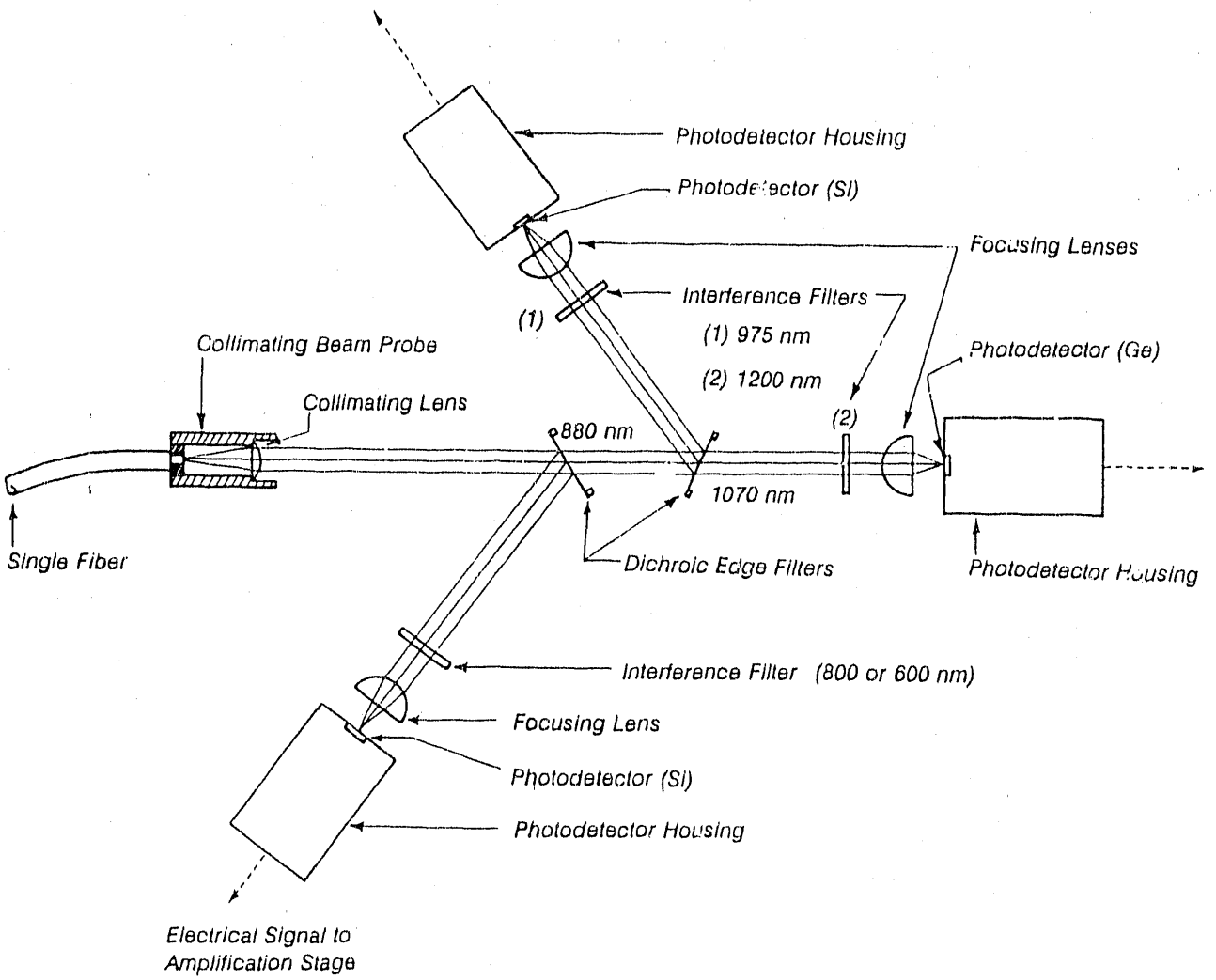

Figure 8. Three-color near infrared optical pyrometer, arrangement of the optics.

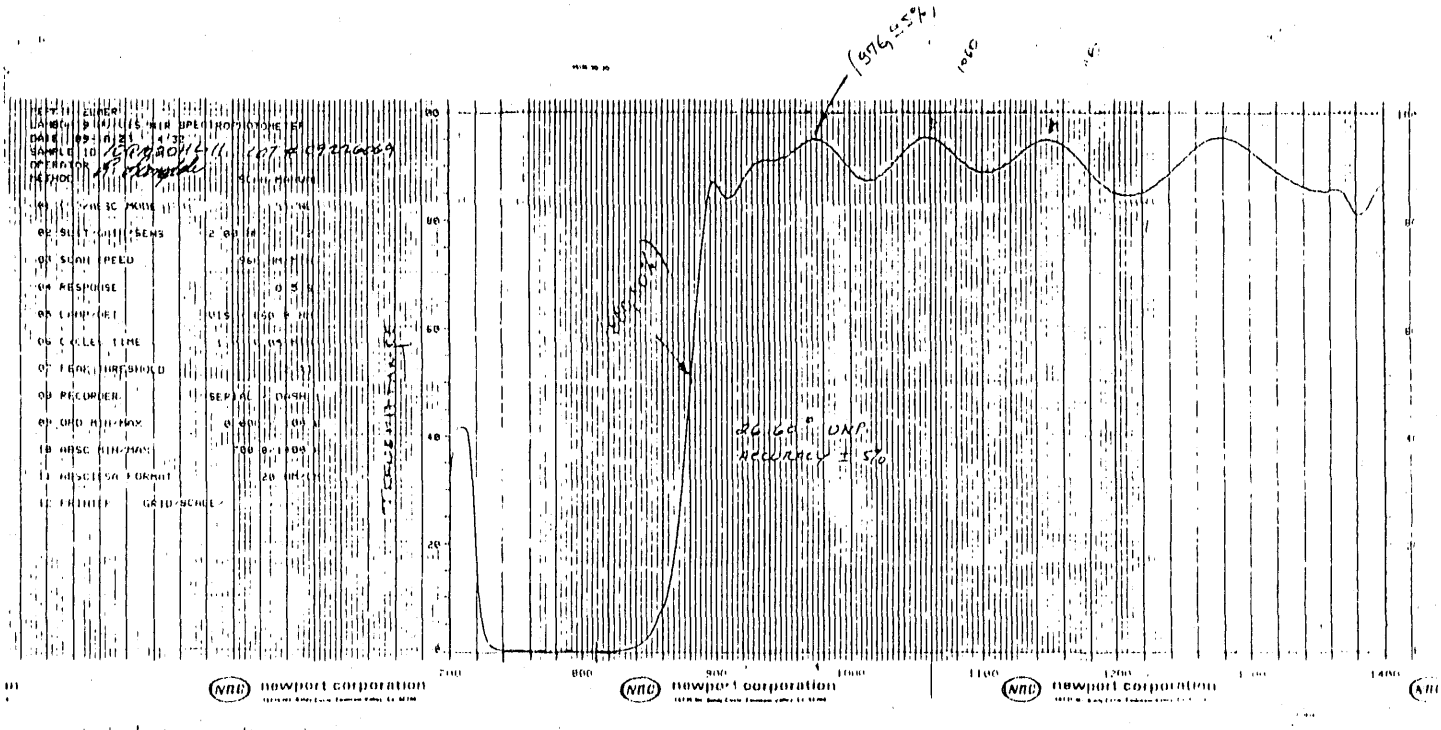

. Figure 9. Radiation spectrum of the first dichroic filter.

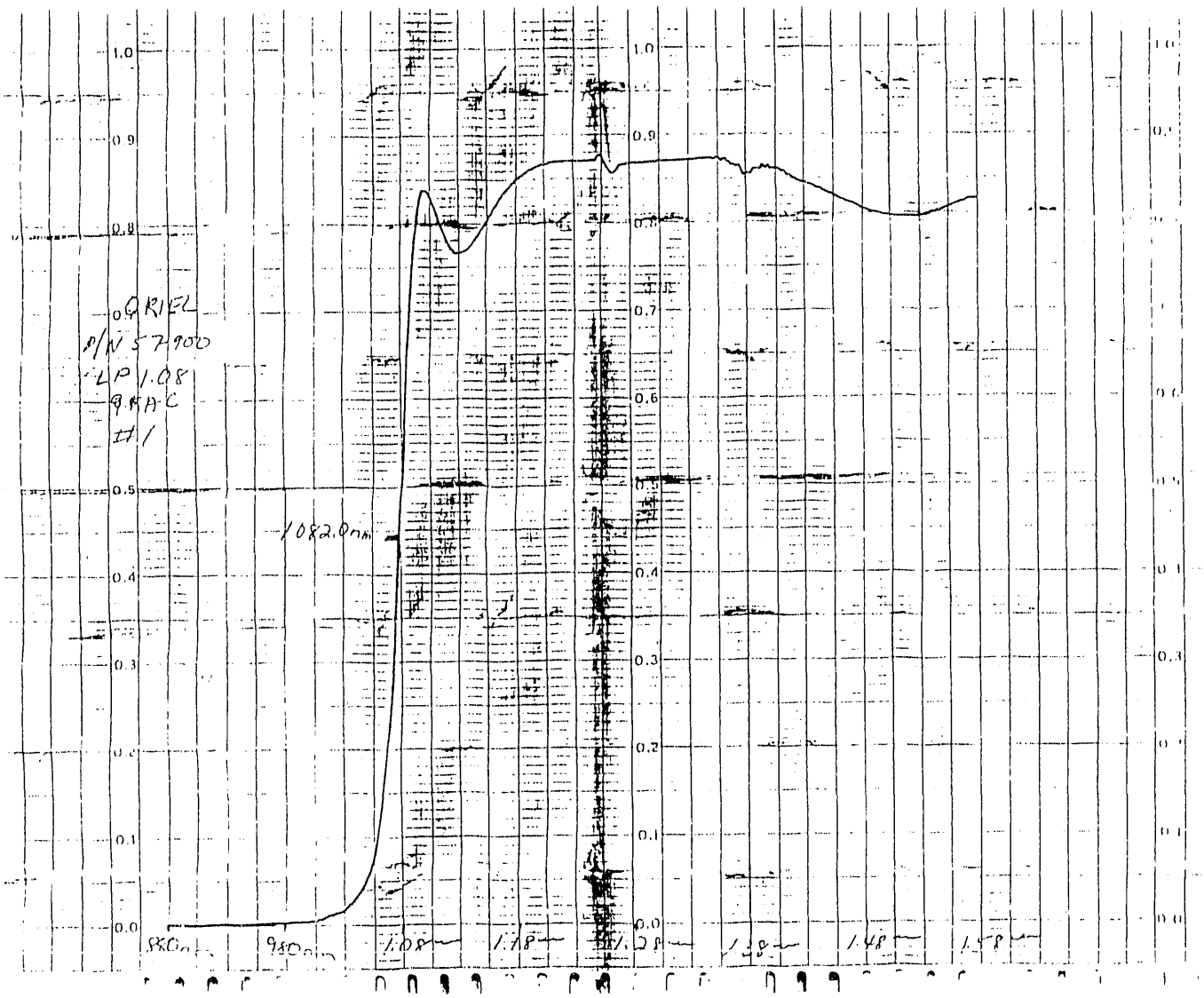

3. Figure 10. Radiation spectrum of the second dichroic filter.

DISCLAIMER

- END

DATE FILM

11 / 29 /